PatchPerPix for Instance Segmentation

Peter Hirsch* Lisa Mais* Dagmar Kainmueller
Berlin Institute of Health / Max-Delbrueck-Center for Molecular Medicine in the Helmholtz Association
{firstname.lastname}@mdc-berlin.de

Abstract

In this paper we present a novel method for proposal free instance segmentation that can handle sophisticated object shapes that span large parts of an image and form dense object clusters with crossovers. Our method is based on predicting dense local shape descriptors, which we assemble to form instances. All instances are assembled simultaneously in one go. To our knowledge, our method is the first non-iterative method that yields instances that are composed of learnt shape patches. We evaluate our method on a diverse range of data domains, where it defines the new state of the art on four benchmarks, namely the ISBI 2012 EM segmentation benchmark, the BBBC010 C. elegans dataset, and 2d as well as 3d fluorescence microscopy datasets of cell nuclei. We show furthermore that our method also applies to 3d light microscopy data of drosophila neurons, which exhibit extreme cases of complex shape clusters.

1. Introduction

The task of instance segmentation has a wide range of applications in natural images as well as microscopy images from the biomedical domain. A prevalent class of instance segmentation methods, namely proposal-based methods based on RCNN [9, 10], has proven successful in cases where instance location and size can be well-approximated by bounding boxes. However, in many cases, especially in the biomedical domain, this does not hold: Instances may span widely across the image, and hence multiple instances may have very similar, large bounding boxes. To complicate things, instances may be densely clustered, in some cases overlapping, including crossovers. Proposal-free methods are applicable in such cases, where popular choices include metric learning / instance coloring [15, 4], affinity-based methods [7, 27, 17, 8], and learnt watershed [3, 28]. However, respective pixel-wise predictions do not explicitly capture instance shape, nor are they suitable for disentangling overlapping instances.

To overcome these limitations, we propose to (1) densely predict representations of the shapes of instance patches, (2) cover the image foreground with the most plausible shape patches, and (3) puzzle together complete instance shapes from these patches by means of partitioning a patch affinity graph. The approach of covering the image by selecting from a redundant set of instance patch predictions allows for naturally handling overlap (including crossovers), as overlapping instance patches can be selected, potentially resulting in pixels covered by multiple instances.

Our general idea is closely related to Singling Out Networks [29]. However, they are different in that they rely on a dictionary of known instances, thereby limiting the variability of objects they can handle, and they only consider predicting whole instances and not patches of instances, thereby limiting the size of feasible object categories.

Our shape prediction network predicts, for each pixel of the input image, a representation of the local shape of the instance this pixel belongs to, namely a *shape patch* of the pixel's instance. The architecture we propose is derived from the U-Net [23], thus allowing for efficient dense prediction. As representations of instance patch shapes, we explore local binary masks, as well as encodings (i.e. compressed versions) of these. The idea of predicting instance shape masks per pixel of an image has been pursued before [5, 6, 13]. However, all these approaches work on the assumption that a shape mask can capture a complete instance shape. Thus they are designed for object categories common to natural images rather than for disentangling clusters of complex shapes that occupy similar bounding boxes, as relevant in the biomedical domain. Predicting shape encodings instead of binary masks is also not new [13]. However, besides only considering complete instance shapes as opposed to our patches of instances, in [13], the shape encoding predictor and the respective decoder are not trained end-to-end, which we show in our work to improve considerably upon separate training.

The variant of our method that predicts local binary masks as shape representations is closely related to methods that employ long-range affinities [14, 27, 17, 8]. In essence, our predicted binary patches can be interpreted as

*equal contribution, listed in random order

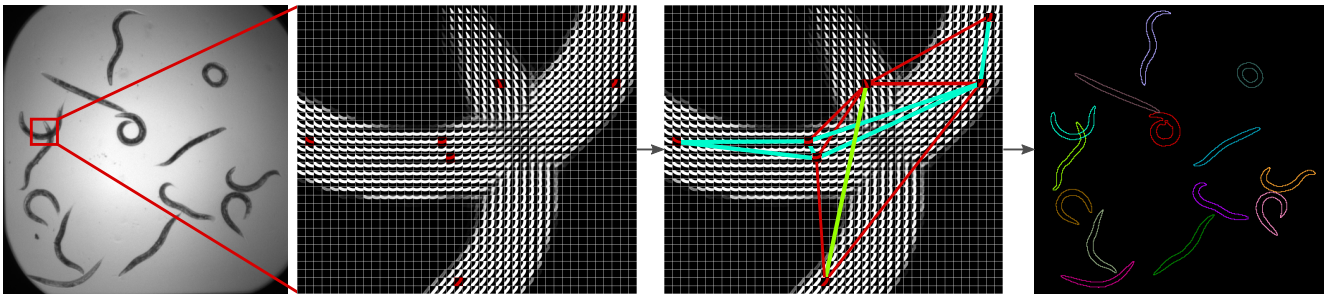

(a) input image (b) predictions, selection (c) patch affinity graph (d) instance seg.

Figure 1: PatchPerPix overview. Given the raw input image (a), a CNN predicts dense patches for each pixel (b, best seen with zoom) which are then used to find a consensus for each pair of pixels within the patch size. The patches that best agree with this consensus are selected (shown in red in b) and connected to form a patch affinity graph. (c) Edges of the patch affinity graph are assigned scores derived from the agreement of the *merged* shape patches with the consensus. The final instance segmentation (d) is obtained by signed graph partitioning. Shown in (c,d) is the result of connected component analysis on the positive subgraph, where edges with negative scores are depicted in red.

dense affinities in a neighborhood around each pixel. However, in contrast to affinity-based methods, we instead interpret our predictions as patches of instances, from which we puzzle together complete instances. This way, our yielded global instance shapes are assembled from *learned shape patches*, a property that does not hold for affinity-based methods. Note that in this respect, our method is related to CELIS [20], which learns to agglomerate super-pixels to form instances with plausible shapes, yet their initial pixel-wise predictions do not capture object shape. Furthermore, our method is related to Flood Filling Networks [11], an iterative method that learns to expand instances one-by-one. In contrast, our method segments all instances simultaneously in one pass.

We show in a quantitative evaluation that our method is the new state of the art on the ISBI 2012 challenge on segmentation of neuronal structures in EM stacks [1], outperforms the previous state of the art [29, 22] on the BBBC010 benchmark microscopy dataset of worms [25] by a large margin, and furthermore also outperforms the state of the art [24, 26] on 2d and 3d light microscopy images of densely packed cell nuclei. Last but not least, we demonstrate that our method also applies to the complex tree-like shapes of neurons in 3d light microscopy images.

In summary, our contributions are:

- A novel method for segmenting instances of complex shapes that spread widely across an image in crowded scenarios, with overlaps and crossovers.
- Instance segmentations are assembled from learnt shape pieces. Our method is, to our knowledge, the first such method that is not iterative, i.e. we compute all instances in one pass.
- Our method defines the new state of the art on the competitive ISBI 2012 EM segmentation challenge, vastly outperforms the state of the art on the challenging BBBC010 C. elegans dataset, and also defines the new state of the art on 2d and 3d benchmark data of cell nuclei.

2. PatchPerPix for Instance Segmentation

We train a CNN to predict dense local shape patches, from which we assemble all instances in an image simultaneously in a one-pass pipeline. Figure 1 provides an overview of our proposed method, which we term *PatchPerPix*.

Formally, our CNN yields an estimate $p\colon \mathrm{Dom}(I)\times\mathcal{P} \to [0,1]$ of the function

$$p^*\colon \mathrm{Dom}(I)\times\mathcal{P}\to\{0,1\}$$
$$(\mathbf{x},\mathbf{dx}) \mapsto \begin{cases} 1 \text{ if } \mathrm{Instance}(\mathbf{x}) = \mathrm{Instance}(\mathbf{x}+\mathbf{dx}) \\ \quad \text{and } \mathbf{x}, \mathbf{x}+\mathbf{dx} \in \mathrm{fg}(I) \\ 0 \text{ otherwise} \end{cases}$$

that captures, for each pixel $\mathbf{x}\in\mathcal{R}^d$ in the foreground $\mathrm{fg}(I)$ of a d-dimensional image I, and each pixel $\mathbf{x}+\mathbf{dx}$ at a fixed, dense set of offsets $\mathcal{P}\subset\mathcal{R}^d$, whether $\mathbf{x}$ and $\mathbf{x}+\mathbf{dx}$ belong to the same instance.

Section 2.1 describes our proposed instance assembly pipeline given the estimated function p. Section 2.2 describes the CNN architectures we explore to yield p.

2.1. Instance Assembly

We denote a restriction of the estimated function p to a single pixel as

$$p_{\mathbf{x}}\colon \mathbf{x}+\mathcal{P}\to[0,1]\,,\ \mathbf{y}\mapsto p(\mathbf{x},\mathbf{y}-\mathbf{x})$$

We denote the domain of $p_{\mathbf{x}}$ as $\text{patch}(p_{\mathbf{x}}) := \mathbf{x} + \mathcal{P}$. For each patch, the pixels that are predicted to belong to the same instance as $\mathbf{x}$ by means of a probability threshold t, i.e. the pixels classified as foreground w.r.t. the instance at $\mathbf{x}$, are denoted as

$$\text{fg}(p_{\mathbf{x}}) := \{\mathbf{y} \in \text{patch}(p_{\mathbf{x}}) : p_{\mathbf{x}}(\mathbf{y}) > t\}\,, \tag{1}$$

and, accordingly, the respective background pixels as

$$\text{bg}(p_{\mathbf{x}}) := \{\mathbf{y} \in \text{patch}(p_{\mathbf{x}}) : p_{\mathbf{x}}(\mathbf{y}) < 1 - t\}\,. \tag{2}$$

For each pixel pair $(\mathbf{y}, \mathbf{z})$ covered by at least one informative patch, i.e. $\exists \mathbf{x} \in \text{Dom}(I) : \{\mathbf{y}, \mathbf{z}\} \subset \text{patch}(p_{\mathbf{x}}) \wedge \{\mathbf{y}, \mathbf{z}\} \cap \text{fg}(p_{\mathbf{x}}) \neq \emptyset$, summing up observations from all patches yields a consensus that $\mathbf{y}$ and $\mathbf{z}$ belong to the same instance, i.e. a consensus affinity

$$\begin{aligned}\text{aff}(\mathbf{y}, \mathbf{z}) := \frac{1}{Z_{\text{aff}}(\mathbf{y}, \mathbf{z})} \cdot \Bigg(& \sum_{\substack{\mathbf{x} \in \text{Dom}(I): \\ \{\mathbf{y}, \mathbf{z}\} \subset \text{fg}(p_{\mathbf{x}})}} p_{\mathbf{x}}(\mathbf{y}) \cdot p_{\mathbf{x}}(\mathbf{z}) \\ - & \sum_{\substack{\mathbf{x} \in \text{Dom}(I): \\ \mathbf{y} \in \text{fg}(p_{\mathbf{x}}), \mathbf{z} \in \text{bg}(p_{\mathbf{x}})}} p_{\mathbf{x}}(\mathbf{y}) \cdot (1 - p_{\mathbf{x}}(\mathbf{z})) \\ - & \sum_{\substack{\mathbf{x} \in \text{Dom}(I): \\ \mathbf{y} \in \text{bg}(p_{\mathbf{x}}), \mathbf{z} \in \text{fg}(p_{\mathbf{x}})}} (1 - p_{\mathbf{x}}(\mathbf{y})) \cdot p_{\mathbf{x}}(\mathbf{z}) \Bigg)\end{aligned} \tag{3}$$

with normalization factor

$$\begin{aligned}Z_{\text{aff}}(\mathbf{y}, \mathbf{z}) := |\{\mathbf{x} \in \text{Dom}(I) : \\ \{\mathbf{y}, \mathbf{z}\} \subset \text{patch}(p_{\mathbf{x}}) \wedge \{\mathbf{y}, \mathbf{z}\} \cap \text{fg}(p_{\mathbf{x}}) \neq \emptyset\}|.\end{aligned} \tag{4}$$

Given these consensus affinities, we define a score for each patch with non-empty foreground by assessing how well it agrees with the consensus:

$$\begin{aligned}\text{score}(p_{\mathbf{x}}) := & \frac{1}{Z_{\text{score}}(p_{\mathbf{x}})} \cdot \\ & \Bigg(\sum_{\{\mathbf{y}, \mathbf{z}\} \subset \text{fg}(p_{\mathbf{x}})} \text{aff}(\mathbf{y}, \mathbf{z}) - \sum_{\substack{\mathbf{y} \in \text{fg}(p_{\mathbf{x}}), \\ \mathbf{z} \in \text{bg}(p_{\mathbf{x}})}} \text{aff}(\mathbf{y}, \mathbf{z}) \Bigg)\end{aligned} \tag{5}$$

with normalization factor

$$Z_{\text{score}}(p_{\mathbf{x}}) := |\{\{\mathbf{y}, \mathbf{z}\} \subset \text{patch}(p_{\mathbf{x}}) : \{\mathbf{y}, \mathbf{z}\} \cap \text{fg}(p_{\mathbf{x}}) \neq \emptyset\}|.$$

We rank all patches w.r.t. their score (Eq. 5). We employ a greedy set cover algorithm to select high-ranking patches whose patch foregrounds $\text{fg}(p_{\mathbf{x}})$ fully cover the image foreground $\text{fg}(I)$. Section 2.2 describes how we obtain the image foreground. In more detail, the set cover algorithm proceeds as follows: Iterating from high to low score over the ranked list of patches, we pre-select patches if they cover previously uncovered image foreground, until the image foreground is fully covered. We further thin out this pre-selection as follows: We iteratively select as next patch from the pre-selection the patch that covers the most remaining foreground, until the whole foreground is covered.

Given this selection of high-ranking patches, the consensus affinities (Eq. 3) allow us to define a score that measures for a *pair of patches* whether they belong to the same instance, i.e. a consensus affinity between $p_{\mathbf{x}}$ and $p_{\mathbf{y}}$:

$$\text{paff}(p_{\mathbf{x}}, p_{\mathbf{y}}) := \frac{1}{Z_{\text{paff}}(p_{\mathbf{x}}, p_{\mathbf{y}})} \cdot \sum_{\substack{\mathbf{v} \in \text{fg}(p_{\mathbf{x}}), \\ \mathbf{w} \in \text{fg}(p_{\mathbf{y}})}} \text{aff}(\mathbf{v}, \mathbf{w}) \tag{6}$$

with normalization factor

$$\begin{aligned}Z_{\text{paff}}(p_{\mathbf{x}}, p_{\mathbf{y}}) := |\{\mathbf{v} \in \text{fg}(p_{\mathbf{x}}), \mathbf{w} \in \text{fg}(p_{\mathbf{y}}) : \\ \exists \mathbf{z} : \{\mathbf{v}, \mathbf{w}\} \subset \text{patch}(p_{\mathbf{z}}) \wedge \{\mathbf{v}, \mathbf{w}\} \cap \text{fg}(p_{\mathbf{z}}) \neq \emptyset\}|.\end{aligned}$$

We compute patch pair affinities (Eq. 6) between selected high-ranking patches iff the respective $Z_{\text{paff}}(\cdot, \cdot) > 0$, yielding a patch affinity graph. We partition this graph via connected component analysis on the positive subgraph, or alternatively by means of the mutex watershed algorithm [27], depending on the application domain. We obtain the final instance segmentation by assigning, per connected component, a unique instance ID to all pixels contained in the union of the respective patch foregrounds. Note that in general, this may assign multiple instance IDs to some pixels, which is desired in some, but not all, applications. In case overlapping instances are not desired, we assign the ID of the patch prediction with highest probability at the respective pixel.

We implemented the computationally expensive parts of our instance assembly pipeline in CUDA for efficient execution. In applications with sparse image foreground, we further improve computational efficiency by restricting $\text{patch}(p_{\mathbf{x}})$ to the image foreground, i.e. $\text{patch}_{\text{sparse}}(p_{\mathbf{x}}) := \text{patch}(p_{\mathbf{x}}) \cap \text{fg}(I)$.

2.2. CNN Architecture

We train a deep convolutional neural network to predict the function p. It does so by predicting $p_{\mathbf{x}}(\mathbf{x} + \mathcal{P})$ for each pixel of the input image. Thus the cardinality of the set $\mathcal{P}$ determines the number of output channels of the network. We train the network w.r.t. standard cross-entropy loss averaged over all outputs. We use a U-Net [23] as backbone architecture. To facilitate predictions of shape representations with hundreds of dimensions, we keep the number of feature maps fixed (instead of reducing) in the upward path of the U-Net. Thus we avoid over-compressing information in the penultimate layer of the U-Net, i.e. we avoid having to predict pixel-wise outputs with hundreds of dimensions from only tens of feature maps.

Our baseline PatchPerPix architecture, termed **ppp**, is a U-Net that directly outputs $p_{\mathbf{x}}$ at each pixel $\mathbf{x}$ of the input

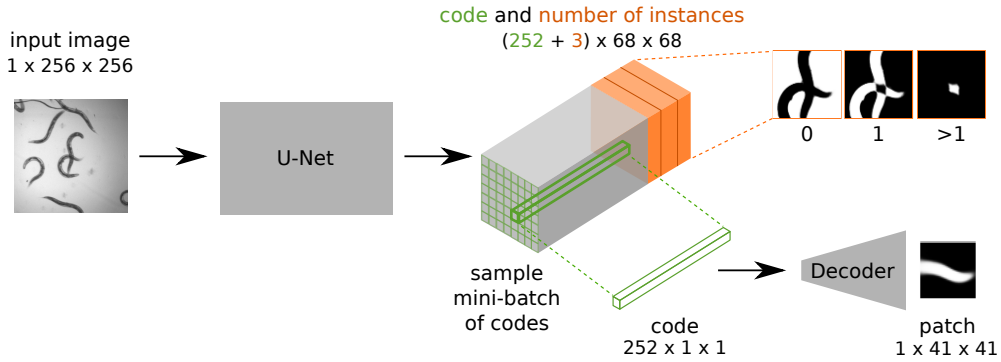

Figure 2: **ppp+dec architecture:** A U-Net predicts shape patch encodings, which are fed into the decoding path of an auto-encoder. Additional outputs of the U-Net predict the number of instances at each pixel. U-Net and decoder are trained jointly end-to-end. Categorical cross-entropy is used for the number of instances, and binary cross-entropy for the patch predictions. Both losses are summed up without weighting. The batch of codes that is run through the decoder is sampled from pixels for which the number of instances is predicted to be 1.

image I. To estimate the image foreground $\text{fg}(I)$, we include offset $\mathbf{0}$ in $\mathcal{P}$.

In most application domains, the variety of possible patch predictions, and hence the amount of information contained in each, is limited. Furthermore, a practical issue with ppp is that the size of the predicted patches, i.e. the number of outputs of the U-Net, is limited by GPU memory. Therefore, in addition to our baseline model, we explore two extensions that learn compressed representations of $p_{\mathbf{x}}$: (1) ppp combined with a separately trained autoencoder (ppp+ae) and (2) ppp plus a decoder, trained end-to-end (ppp+dec), as described in the following.

ppp+ae. In a separate first step, we train a fully convolutional autoencoder on patches of the ground truth binary masks to learn a patch latent space. The baseline U-Net is then trained to regress a respective learnt latent code vector for each pixel of the input image. This modified architecture is trained w.r.t. sum of squared differences loss averaged over the predicted code vectors. To generate uncompressed patch predictions to be fed into our instance assembly pipeline, the decoder part of the pre-trained autoencoder is employed to decompress the encoded vectors. To this end, we add an extra output channel to the U-Net to predict the foreground mask. This is trained using the cross-entropy loss and added to the code loss without any weighting. The codes are decoded for all foreground pixels obtained by thresholding the foreground mask.

ppp+dec. Here, we attach the decoder part of the autoencoder used in ppp+ae to the end of the U-Net and train the resulting joint network end-to-end from scratch w.r.t. cross-entropy as in ppp. As before, the U-Net part of the network outputs the code. However, there is no loss employed directly on the code. To fit end-to-end training onto GPU memory, we sample codes from ground truth foreground pixels at training time, which are then fed to the decoder network. Similarly to ppp+ae, we extend the U-Net to simultaneously predict the foreground to allow decoding only for foreground pixel while testing. This architecture is depicted in Figure 2.

ppp+dec combines a U-Net for predicting a shape encoding with the decoder part of an auto-encoder. Interestingly, this end-to-end trainable architecture has two decoding parts, namely (1) the upward path of the U-Net, which serves for combining high-level image information captured at lower layers with low-level information from upper layers, and (2) the decoder half of an auto-encoder, which is needed to decompress local shape predictions in the end. Furthermore, especially when dealing with sparse data, the U-Net performs many dispensable computations, namely on background pixels. This opens up the question whether our proposed architecture could not be replaced by a standard encoder-decoder architecture alone, with one encoding and one decoding path, like e.g. [2]. We investigated this alternative as follows:

ed-ppp. Our architecture takes an image patch the size of our shape patches plus some surrounding receptive field as input, and generates a shape patch for the respective central pixel's instance as output. It is applied in a sliding window fashion on all pixels in the image foreground. We use 3×3 down- and upsampling to facilitate the singling out of the center pixel's instance from its neighboring instances. To determine for which pixels to run the encoder-decoder network, we train a separate U-Net to generate a foreground mask in a preceding step.

2.3. Overlapping Regions

The case of multiple objects sharing pixels can be found in many biomedical applications, e.g. in 2d images of model organisms such as worms that crawl on top of each other, or neurons in light microscopy data that share pixels due to the

partial volume effect. As pixels located in areas of overlap belong to multiple instances, their respective shape patch is not well-defined. Hence we exclude these pixels from the entire pipeline.

During training, we achieve this by masking out these areas in the loss computation. To detect overlap at test time, we predict the number of instances per pixel by extending the foreground classification task by an "overlap" class, which, as before, is trained jointly with the patch predictions by means of added cross-entropy loss. This information is then used in the instance assembly: Pixels in overlapping regions are discarded, i.e. their respective shape patches do not contribute to the consensus and cannot be selected. In consequence, this constitutes a limitation of our method in that (i) only overlapping regions with a maximum diameter of smaller than the size of the patches can be covered completely by patch shapes, and (ii) only occlusions within the range of the neighborhood used in the patch graph generation can be bridged.

3. Results

We evaluate our method on four benchmark datasets, which comprise overlapping objects, sophisticated object shapes, and, to show the generic applicability of our method, also simple object shapes. The first dataset, the BBBC010 C. elegans dataset [18], exhibits clusters of overlapping objects with large, coinciding bounding boxes. The second dataset, the ISBI 2012 Challenge on segmenting neuronal structures in electron microscopy [1], exhibits densely clustered objects with sophisticated shapes that span the whole image, albeit without overlaps. The third and fourth dataset exhibit densely clustered objects of simple, approximately ellipsoidal shapes, namely 2d and 3d fluorescence light microscopy datasets of cell nuclei [24, 26].

Our results define the new state of the art in all cases, as detailed in Sections 3.1, 3.2, and 3.3. Furthermore, we study the impact of individual steps of our instance assembly pipeline as well as our proposed network architecture designs on BBBC010, as detailed in Section 3.1. Last, we show promising qualitative results of our method on 3d light microscopy data of neurons, which exhibit extreme cases of sophisticated object shapes that form dense clusters with overlaps (Sec. 3.4).

3.1. BBBC010 C. elegans worm disentanglement

The **BBBC010** dataset, available from the Broad Bioimage Benchmark Collection [18][1], consists of 100 brightfield microscopy images showing multiple C. elegans worms per image, which may overlap and cluster. As ground truth, to capture overlaps correctly, BBBC010 provides an individual binary mask for each worm.

[1]BBBC010v1: C.elegans infection live/dead image set version 1 provided by Fred Ausubel

In this section we report a comparison of our method with related work [29, 22]. Furthermore, we report a comparison of the neural network architecture designs we explored, as well as an ablation study that assesses the impact of individual steps of our instance assembly pipeline. We report results in terms of the AP_{dsb} metric used in the kaggle 2018 data science bowl ($AP_{dsb} = \frac{TP}{TP+FP+FN}$) which takes both missing and spurious instances into account[2]. Furthermore, we also report a range of additional metrics that have been reported by competing approaches, including the slightly different AP_{COCO}, thus enabling direct comparability to related work.

As backbone CNN architecture we employ a 4-level U-Net [23] starting with 40 feature maps, with two-fold down- and upsampling operations, and constant number of feature maps during upsampling. Our network takes raw brightfield images as sole input, while [22] and [29] additionally exploit ground truth segmentations of the image foreground as input. In the ppp architecture, we employ a patch size of 25×25, yielding a U-Net with 625 outputs. In the ppp+ae and ppp+dec architectures, we employ a code of size 252 as intermediate output of the U-Net, which is then fed into a decoder network to yield a patch of size 41×41. The ed-ppp architecture takes 81×81 patches of the raw image as input and predicts 41×41 shape patches. It applies 3×3 max-pooling three times, and has two convolutional layers on each level. At the bottleneck, the code has an extent of $3 \times 3 \times 256$ and uses 1×1 convolutions. The network is symmetric and uses same padding. The output is cropped to obtain the desired patch shape.

As in related work [29, 22], we divide the BBBC010 dataset into a training and testing set with 50 images each, and apply 2-fold cross-validation on the testing set. We determine the number of training steps as well as the patch foreground threshold t (Eq. 1) in all experiments individually via the validation sets. For training, we use standard augmentation by rotation, mirroring and elastic deformations in all experiments. Contrary to [29], we do not augment the number of worms synthetically, but focus on crowded regions during training. For partitioning the patch graph, we explore connected component analysis on the positive subgraph (CC) as well as the mutex watershed (MWS) [27]. In our result tables, MWS is the default if not noted otherwise.

The comparison to state-of-the-art methods [22, 29] and between our CNN architectures are shown in Table 1. Results of our ablation study are listed in Table 2. Figure 3 shows exemplary PatchPerPix results for different CNN architectures. Figure 4 shows a comparison of PatchPerPix (ppp+dec) with Singling Out Networks [29] on an exemplary image.

PatchPerPix (ppp+dec) improves over competing meth-

[2]https://www.kaggle.com/c/data-science-bowl-2018

BBBC010						
AP_{COCO}	$avAP_{[0.5:0.05:0.95]}$	$AP_{0.5}$	$AP_{0.75}$	$Recall_{0.5}$	$Recall_{0.8}$	$F1_{0.8}$
Semi-conv Ops [22]	0.569	0.885	0.661	-	-	-
SON [29]	-	-	-	~ 0.97	~ 0.7	-
WormToolbox [25]	-	-	-	-	-	0.81
PatchPerPix (ppp+dec)	**0.783**	**0.943**	**0.897**	**0.987**	**0.890**	**0.978**

AP_{dsb}	$avAP_{[0.5:0.05:0.95]}$	$AP_{0.5}$	$AP_{0.6}$	$AP_{0.7}$	$AP_{0.8}$	$AP_{0.9}$
ppp	0.689	0.890	0.872	0.840	0.710	0.372
ppp+ae	0.617	0.873	0.833	0.790	0.609	0.198
ppp+dec	**0.735**	**0.934**	**0.907**	**0.890**	**0.786**	**0.408**
ed-ppp	0.681	0.891	0.860	0.832	0.743	0.311

Table 1: Quantitative results on the BBBC010 dataset. Top: We compare to competing approaches in various metrics due to a missing standard. [22] report COCO evaluation metrics [16]. [29] plot the recall for different thresholds. [25] evaluate the percentage of ground truth worms which are matched with pixelwise F1 score above 0.8. Bottom: Results for the architecture setups we explored. ppp+dec trained end-to-end considerably outperforms the other setups.

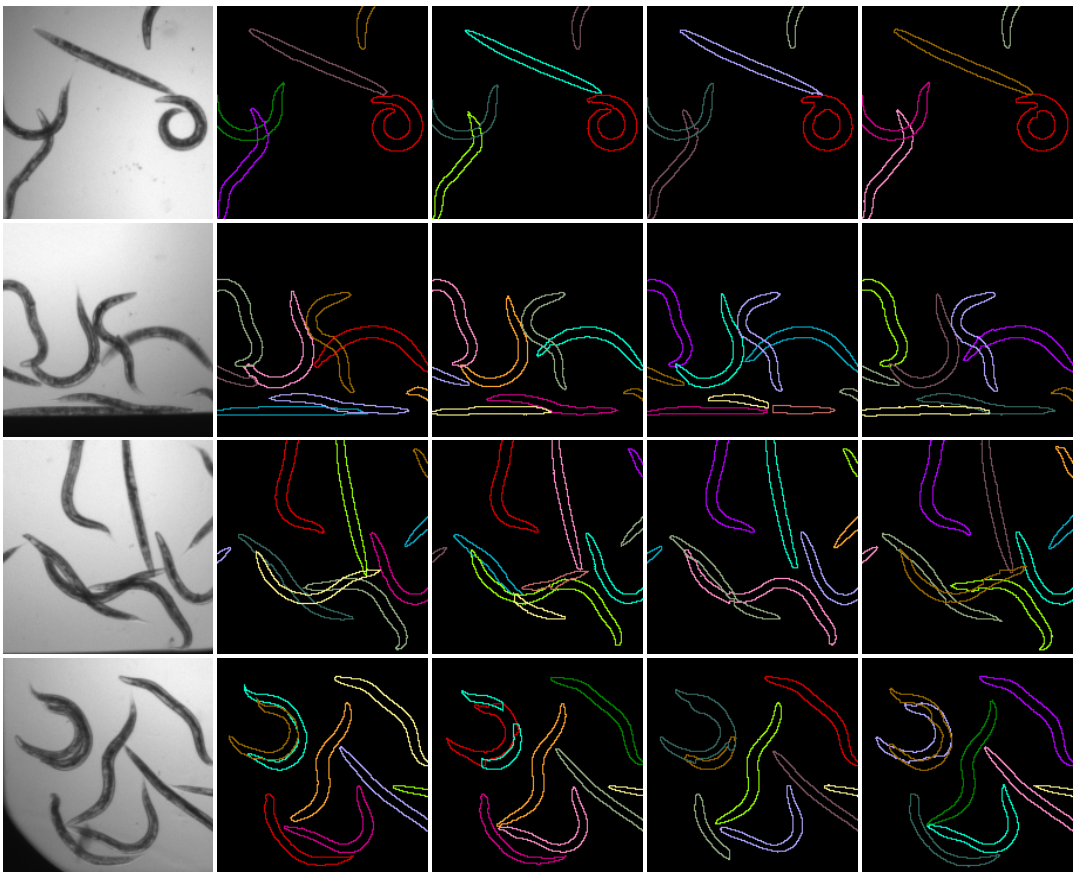

(a) raw (b) gt (c) ppp (d) ed-ppp (e) ppp+dec

Figure 3: Qualitative results for exemplary challenging regions of the BBBC010 dataset. All architectures are able to handle crowded and overlapping regions, where ppp+dec yields fewest errors. ppp yields a higher number of false splits, which may be due to a smaller patch size. However, rare shapes such as very bent worms are segmented with slightly higher accuracy.

AP_{dsb}	$avAP_{[0.5:0.05:0.95]}$	$AP_{0.5}$	$AP_{0.6}$	$AP_{0.7}$	$AP_{0.8}$	$AP_{0.9}$
MWS-Dense	0.552	0.686	0.677	0.663	0.589	0.317
ppp+dec w/o selection	0.612	0.906	0.874	0.834	0.597	0.147
ppp+dec w/o thinout	0.725	0.922	0.900	0.881	0.777	0.400
ppp+dec std U-Net	0.722	0.915	0.894	0.872	0.778	0.402
ppp+dec, CC	0.734	**0.935**	0.900	0.886	**0.789**	**0.413**
ppp+dec, MWS	**0.735**	0.934	**0.907**	**0.890**	0.786	0.408

Table 2: Ablation study for PatchPerPix on the BBBC010 dataset. We ablate consensus affinity computation as a whole by running graph partitioning directly on the predictions p interpreted as dense affinities (MWS-Dense). We ablate patch selection as a whole (ppp+dec w/o selection), and thinning of the patch selection (ppp+dec w/o thinout). Furthermore, we run ppp+dec with a standard U-Net, i.e. without keeping the number of feature maps constant in the up-sampling path (ppp+dec std U-Net). Last, we compare patch graph partitioning with CC vs. MWS.

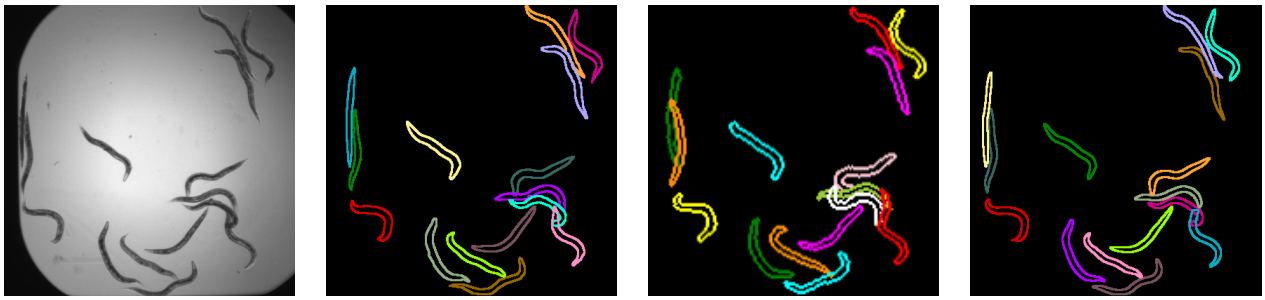

(a) raw (b) ground truth (c) SON (d) PatchPerPix

Figure 4: Qualitative comparison of PatchPerPix and Singling Out Networks [29] (SON) on a BBBC010 image. PatchPerPix (ppp+dec) is significantly more pixel-accurate overall as it does not rely on a dictionary of known shapes. In particular, PatchPerPix accurately separates a cluster of objects on the lower right. (SON image from [29])

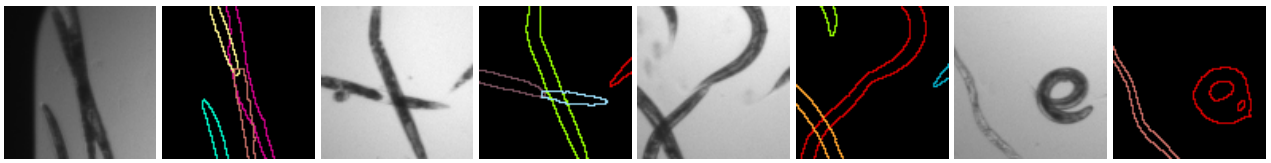

Figure 5: Exemplary failure cases of PatchPerPix (ppp+dec) on BBBC010. From left to right: false split due to large overlap; false split due to missing signal; false merge due to sequential arrangement of worms; inaccuracy due to strongly bent worm.

ods by a large margin (cf. Table 1, top). Singling Out Networks (SON [29]) are of limited pixel accuracy by design, hence superior performance of PatchPerPix at high IoU thresholds is no surprise. However, PatchPerPix is not just more pixel accurate, but outperforms SON across the IoU threshold range.

Interestingly, ppp+dec does not just outperform the separately trained ppp+ae, but also outperforms ed+ppp. I.e., *using a full U-Net as an encoder,* followed by a standard decoder, considerably outperforms a standard encoder-decoder architecture applied in a sliding-window fashion (cf. Table 1, bottom).

Our ablation study (Table 2) shows the significant impact of two core ideas of our instance assembly pipeline, namely consensus affinity computation (absent in MWS-Dense, avAP -0.183) and selecting a sparse set of high-ranking predictions while weeding out low-ranking predictions by means of consensus agreement score (absent in ppp+dec w/o selection, avAP - 0.123). Thinning out the pre-selection of high ranking patches has a smaller impact on accuracy (ppp+dec w/o thinout, avAP - 0.010), yet also has a positive impact on computational performance. Patch graph partitioning via CC vs. MWS are on a par on the BBBC010 data.

Figure 5 shows exemplary failure cases of ppp+dec. Interestingly, strongly bent worms are captured with inferior pixel accuracy by our encoding-based model ppp+dec as opposed to baseline ppp (see Fig. 5 right and Fig. 3 top row).

3.2. ISBI 2012 neuron EM segmentation

We evaluate our method on the ISBI 2012 Challenge on segmenting neuronal structures in electron microscopy (EM) data [1]. The data consists of 30 slices of 512x512 pixels with known ground truth (training data), and another 30 such slices for which ground truth is kept secret by the Challenge organizers (test data). Our network architecture as well as the training- and prediction procedure closely follows [27], with the difference that our network has 625 instead of 17 outputs, namely patches of size 1x25x25, and we do not reduce the number of filters in the upward path of the U-Net. For partitioning the patch graph, we use the mutex watershed algorithm [27], which has proven powerful in avoiding false mergers in case of missing neuron membrane signal in the image data.

Our method is the leading entry on the Challenge's leaderboard[3] at present among thousands of submissions by more than 200 teams. Table 3 lists results obtained with PatchPerPix in terms of the Challenge error metrics, robust Rand score (rRAND) and robust information theoretic measure (rINF), evaluated on the test data. For comparison, the table also lists the previous state of the art as obtained via sparse affinity predictions processed with the mutex watershed algorithm [27] (MWS). Furthermore, besides processing our patch predictions with the proposed instance assembly pipeline, as an additional baseline, we interpreted them as dense affinities which we processed with the mutex watershed algorithm as in [27] (MWS-Dense). PatchPerPix slightly outperforms MWS in terms of the leaderboard-defining rRAND score. This can be attributed to fewer mistakes on large neuronal bodies which have respective large impact on the rRAND score. However, the number of such large mistakes we were able to identify by eye on the test set is very small (at most three) in both approaches.

Interestingly, MWS-Dense performs considerably worse than both PatchPerPix and MWS. The difference between MWS-Dense and PatchPerPix can be attributed to individual erroneous predictions causing errors in MWS-Dense, which are amended in PatchPerPix by our proposed consensus voting and patch selection scheme. As for the difference between MWS-Dense and MWS, we hypothesize that this is due to MWS smartly distinguishing between purely attractive short-range- and purely repulsive long-range affinities. Instead, MWS-Dense treats all affinities as both attractive and repulsive.

3.3. Nuclei segmentation in 2d and 3d

We evaluate our method on 2d and 3d fluorescence microscopy images of cell nuclei. The 2d dataset is a subset of the kaggle 2018 data science bowl[4] as defined in [24]. The training set consists of 447 and the test set of 50 images. We refer to this dataset as **dsb2018**. The 3d dataset consists of 28 confocal microscopy images collected and annotated by [19]. Image size is approximately $140 \times 140 \times 1100$ pixels. Each image shows hundreds of nuclei, with multiple dense clusters. An example is shown in Figure 6. This data has been used as benchmark data in [26], with 18 volumes for training, 3 for validation, and 7 for testing. We refer to this dataset as **nuclei3d**.

For dsb2018, our CNN architecture is a 4-level U-Net, with 64 initial feature maps, that predicts patches of size of 25×25. As additional, auxiliary training task, we regress for each pixel a vector to the center pixel of its instance. We perform 2-fold cross validation to determine the number of training steps as well as the patch threshold. For nuclei3d, we employ a 3-level 3d U-Net with 20 initial feature maps, tripled after each downsampling step. We predict patches of size $9 \times 9 \times 9$. We filter out instances smaller than a threshold. We determine the number of training steps, patch threshold, and instance size threshold on the validation set.

Table 4 lists our results in comparison to the previous state of the art [24, 26]. Superior avAP of PatchPerPix can mainly be attributed to superior performance at high IoU thresholds. The latter is not surprising, as StarDist [24, 26] is based on coarse polyhedral shape representation, which limits the achievable pixel accuracy especially in 3d. We list IoU thresholds down to 0.1 as in [26], which indicate that PatchPerPix is on a par with StarDist in terms of grave segmentation errors like false splits and false mergers of nuclei on the 3d data.

ISBI2012	rRAND	rINF
PatchPerPix	**0.988290**	0.991544
MWS [27]	0.987922	**0.991833**
MWS-Dense	0.979112	0.989625

Table 3: Quantitative results for the ISBI 2012 Challenge on segmenting neuronal structures in electron microscopy data [1]. PatchPerPix defines the current state-of-the-art in terms of the leaderboard-defining rRAND score. For comparison, we list the previous state of the art (MWS [27]), as well as a baseline that applies MWS to our patch predictions interpreted as dense pixel affinities (MWS-Dense).

3.4. Neuron separation in 3d light microscopy data

We aim to identify and segment neurons of the fruit fly brain (GAL4 lines [12]) in an unpublished dataset of 3d multicolor confocal microscopy images. The imaging is done by stochastic labeling able to express different densities of neurons [21] (cf. Fig. 7a). This instance segmentation task is very challenging as the number of neurons can

[3] http://brainiac2.mit.edu/isbi_challenge/leaders-board-new

[4] BBBC038v1: available from the Broad Bioimage Benchmark Collection[18]

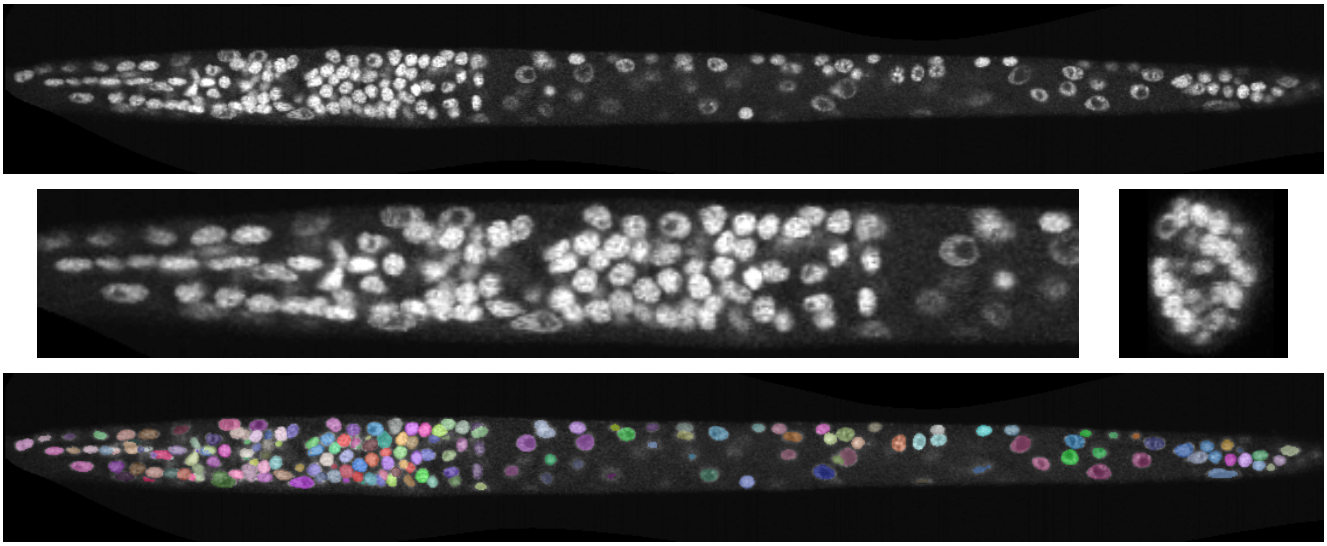

Figure 6: Top: Exemplary xy-slice of a volume in the nuclei3d data set. Densely packed nuclei in the nervous system of the C. elegans L1 larva (towards the left) are particularly hard to separate. Center left: Close-up on said nervous system. Center right: Exemplary yz-slice of nervous system. Bottom: Respective PatchPerPix segmentation result.

AP_{dsb}	avAP [0.5:0.1:0.9]	$AP_{0.1}$	$AP_{0.2}$	$AP_{0.3}$	$AP_{0.4}$	$AP_{0.5}$	$AP_{0.6}$	$AP_{0.7}$	$AP_{0.8}$	$AP_{0.9}$
					dsb2018					
Mask R-CNN[24]	0.594	-	-	-	-	0.832	0.773	0.684	0.489	0.189
StarDist[24]	0.584	-	-	-	-	0.864	0.804	0.685	0.450	0.119
PatchPerPix	**0.680**	0.920	0.919	0.915	0.904	**0.869**	**0.820**	**0.752**	**0.612**	**0.349**
					nuclei3d					
IFT-WS[26]	0.227	0.794	0.771	0.708	0.601	0.472	0.364	0.222	0.074	0.005
U-Net+WS[26]	0.370	0.920	0.905	0.872	0.807	0.700	0.593	0.406	0.144	0.005
StarDist 3D[26]	0.406	**0.936**	**0.926**	0.905	0.855	**0.765**	0.647	0.460	0.154	0.004
PatchPerPix	**0.434**	0.933	**0.926**	**0.906**	**0.862**	0.763	**0.670**	**0.498**	**0.216**	**0.021**

Table 4: Quantitative results for the nuclei datasets dsb2018 and nuclei3d. We report average precision (AP_{dsb}) for multiple IoU thresholds. At lower IoU thresholds, PatchPerPix is slightly better (2d) or on par (3d) with the state of the art [24, 26]. At higher thresholds, in both 2d and 3d, improvement over the state of the art is considerable.

be high and image quality is bounded by the necessity to perform large-scale imaging. Moreover, the neurons are very thin, tree-like structures which are intertwined and may overlap due to partial volume effects.

As this dataset is still in the process of being curated and extended, and no competing approach has yet been reported, we do not perform a quantitative evaluation of PatchPerPix, but show the quality of exemplary results on a test set of two images in Figure 7. We use a 3-level 3d U-Net with $2\times$ down- and upsampling and 12 initial feature maps, tripled at each downsampling. The predicted patches are of size $7 \times 7 \times 7$ pixels. Our results serve as proof-of-concept that our method is applicable and yields reasonable results for thin, complex tree-like structures in large 3d image volumes.

4. Conclusion

In this work we present a novel generic method for instance segmentation that comprises a CNN to predict dense local shape descriptors and a one-pass instance assembly pipeline. The method is able to handle objects of sophisticated shapes that appear in dense clusters with overlaps, including crossovers. It is the first to assemble all instances from learnt shape patches, simultaneously in one pass. We successfully applied our method to a range of domains,

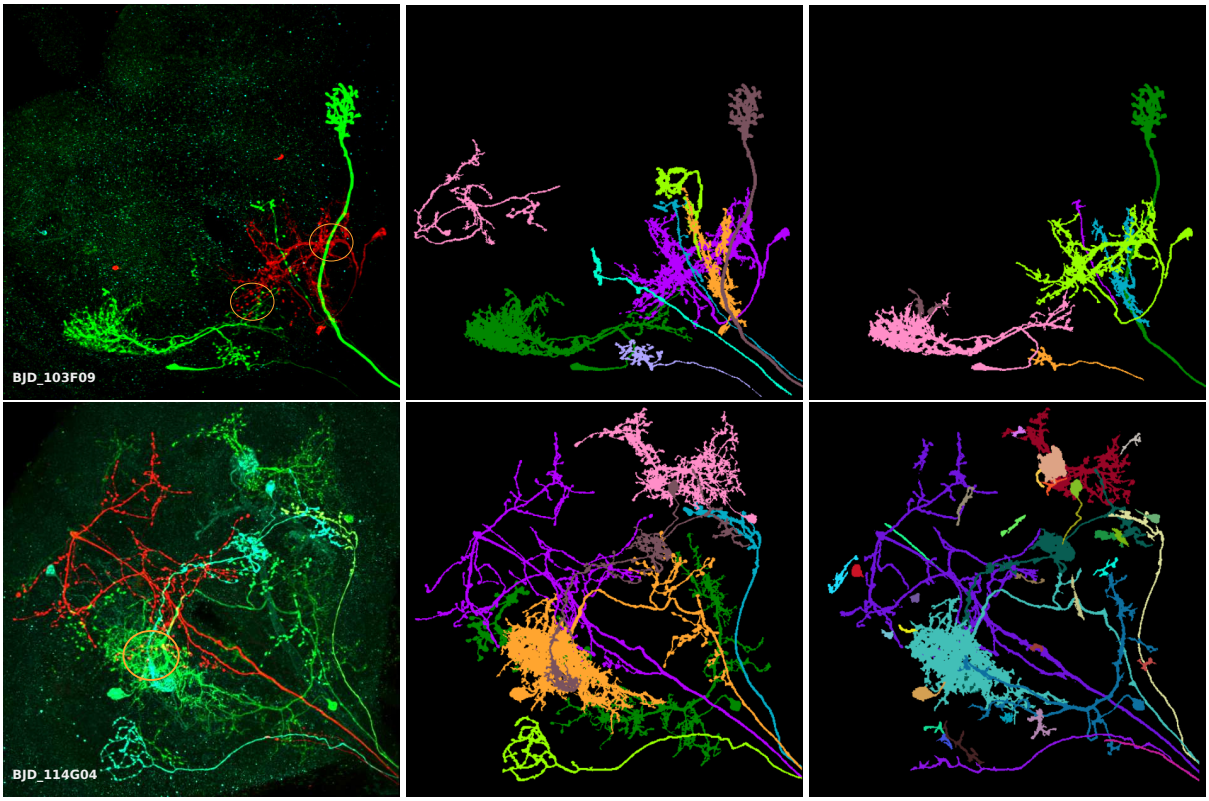

(a) raw (b) gt (c) ppp

Figure 7: Qualitative results on 3d neuron light microscopy examples. (a) Raw images, visualized via maximum intensity projection. Orange circles indicate overlapping areas in 3d. Ground truth data (b) were generated by manual segmentation using VVD Viewer. PatchPerPix (c) shows promising results on this challenging dataset.

showing that it

1. Outperforms the state of the art on the heavily contested ISBI 2012 challenge on neuron segmentation in electron microscopy,

2. Outperforms the state of the art on the challenging BBBC010 C. elegans worm data by a large margin,

3. Outperforms the state of the art on 2d and 3d fluorescence microscopy data of densely clustered cell nuclei, showing that our method is generic in that it performs well also for simple (blob-like) instance shapes, and

4. Can be applied to extreme cases of instance shapes, like neurons in 3d fluorescence microscopy volumes.

Future work will include semantic object labels in our models. Furthermore, shape patches predicted by our baseline architecture appear as flattened tensors neglecting their 2d or 3d spatial nature, which recently has been shown to not fully leverage local structure, with suggested alternatives that we will explore [5].

Acknowledgments

We wish to thank Constantin Pape for his invaluable help in reproducing the network architecture and training- and prediction procedure from [27]. Many thanks also to Carolina Waehlby for her help with the BBBC010 data, and to Stephan Saalfeld and Carsten Rother for very helpful discussions. Moreover, we want to thank the FlyLight Project Team[5] at Janelia Research Campus for providing the unpublished data and Claire Managan and Ramya Kappagantula (Janelia Project Technical Resources) for their conscientious manual neuron segmentation in fly brain images. P.H., L.M. and D.K. were funded by the Berlin Institute of Health and the Max Delbrueck Center for Molecular Medicine. P.H. was funded by HFSP grant RGP0021/2018-102. P.H., L.M. and D.K. were supported by the HHMI Janelia Visiting Scientist Program. VVD Viewer[6] is an open-source software funded by NIH grant R01-GM098151-01.

[5] https://www.janelia.org/project-team/flylight
[6] https://github.com/takashi310/VVD_Viewer

References

[1] Ignacio Arganda-Carreras, Srinivas C Turaga, Daniel R Berger, Dan Cireşan, Alessandro Giusti, Luca M Gambardella, Jürgen Schmidhuber, Dmitry Laptev, Sarvesh Dwivedi, Joachim M Buhmann, et al. Crowdsourcing the creation of image segmentation algorithms for connectomics. *Frontiers in neuroanatomy*, 9:142, 2015. 2, 5, 8

[2] Vijay Badrinarayanan, Alex Kendall, and Roberto Cipolla. Segnet: A deep convolutional encoder-decoder architecture for image segmentation. *IEEE transactions on pattern analysis and machine intelligence*, 39(12):2481–2495, 2017. 4

[3] Min Bai and Raquel Urtasun. Deep watershed transform for instance segmentation. *CoRR*, abs/1611.08303, 2016. 1

[4] Long Chen, Martin Strauch, and Dorit Merhof. Instance segmentation of biomedical images with an object-aware embedding learned with local constraints. In *International Conference on Medical Image Computing and Computer-Assisted Intervention*, pages 451–459. Springer, 2019. 1

[5] Xinlei Chen, Ross B. Girshick, Kaiming He, and Piotr Dollár. Tensormask: A foundation for dense object segmentation. *CoRR*, abs/1903.12174, 2019. 1, 10

[6] Jifeng Dai, Kaiming He, Yi Li, Shaoqing Ren, and Jian Sun. Instance-sensitive fully convolutional networks. *CoRR*, abs/1603.08678, 2016. 1

[7] Jan Funke, Fabian Tschopp, William Grisaitis, Arlo Sheridan, Chandan Singh, Stephan Saalfeld, and Srinivas Turaga. Large scale image segmentation with structured loss based deep learning for connectome reconstruction. *IEEE Transactions on Pattern Analysis and Machine Intelligence*, PP:1–1, 05 2018. 1

[8] Naiyu Gao, Yanhu Shan, Yupei Wang, Xin Zhao, Yinan Yu, Ming Yang, and Kaiqi Huang. Ssap: Single-shot instance segmentation with affinity pyramid. In *Proceedings of the IEEE International Conference on Computer Vision*, pages 642–651, 2019. 1

[9] Ross Girshick, Jeff Donahue, Trevor Darrell, and Jitendra Malik. Rich feature hierarchies for accurate object detection and semantic segmentation. In *Proceedings of the 2014 IEEE Conference on Computer Vision and Pattern Recognition*, CVPR '14, pages 580–587, Washington, DC, USA, 2014. IEEE Computer Society. 1

[10] Kaiming He, Georgia Gkioxari, Piotr Dollr, and Ross Girshick. Mask r-cnn, 2017. cite arxiv:1703.06870Comment: open source; appendix on more results. 1

[11] Michal Januszewski, Jeremy Maitin-Shepard, Peter Li, Jörgen Kornfeld, Winfried Denk, and Viren Jain. Flood-filling networks. *CoRR*, abs/1611.00421, 2016. 2

[12] Arnim Jenett, Gerald M. Rubin, Teri-T B. Ngo, David Shepherd, Christine Murphy, Heather Dionne, Barret D. Pfeiffer, Amanda Cavallaro, Donald Hall, Jennifer Jeter, Nirmala Iyer, Dona Fetter, Joanna H. Hausenfluck, Hanchuan Peng, Eric T. Trautman, Robert R. Svirskas, Eugene W. Myers, Zbigniew R. Iwinski, Yoshinori Aso, Gina M. DePasquale, Adrianne Enos, Phuson Hulamm, Shing Chun Benny Lam, Hsing-Hsi Li, Todd R. Laverty, Fuhui Long, Lei Qu, Sean D. Murphy, Konrad Rokicki, Todd Safford, Kshiti Shaw, Julie H. Simpson, Allison Sowell, Susana Tae, Yang Yu, and Christopher T. Zugates. A gal4-driver line resource for drosophila neurobiology. *Cell reports*, 2(4):991–1001, Oct 2012. 23063364[pmid]. 8

[13] Saumya Jetley, Michael Sapienza, Stuart Golodetz, and Philip H. S. Torr. Straight to shapes: Real-time detection of encoded shapes. *CoRR*, abs/1611.07932, 2016. 1

[14] Margret Keuper, Evgeny Levinkov, Nicolas Bonneel, Guillaume Lavoué, Thomas Brox, and Bjorn Andres. Efficient decomposition of image and mesh graphs by lifted multicuts. In *Proceedings of the IEEE International Conference on Computer Vision*, pages 1751–1759, 2015. 1

[15] Kisuk Lee, Ran Lu, Kyle Luther, and H. Sebastian Seung. Learning dense voxel embeddings for 3d neuron reconstruction, 2019. 1

[16] Tsung-Yi Lin, Michael Maire, Serge Belongie, James Hays, Pietro Perona, Deva Ramanan, Piotr Dollár, and C. Lawrence Zitnick. Microsoft coco: Common objects in context. In David Fleet, Tomas Pajdla, Bernt Schiele, and Tinne Tuytelaars, editors, *Computer Vision – ECCV 2014*, pages 740–755, Cham, 2014. Springer International Publishing. 6

[17] Yiding Liu, Siyu Yang, Bin Li, Wengang Zhou, Jizheng Xu, Houqiang Li, and Yan Lu. Affinity derivation and graph merge for instance segmentation. *CoRR*, abs/1811.10870, 2018. 1

[18] Vebjorn Ljosa, Katherine L. Sokolnicki, and Anne E. Carpenter. Annotated high-throughput microscopy image sets for validation. *Nature Methods*, 9:637 EP –, Jun 2012. Correspondence. 5, 8

[19] Fuhui Long, Hanchuan Peng, Xiao Liu, Stuart K. Kim, and Eugene Myers. A 3d digital atlas of c. elegans and its application to single-cell analyses. *Nature Methods*, 6(9):667–672, 2009. 8

[20] Jeremy B Maitin-Shepard, Viren Jain, Michal Januszewski, Peter Li, and Pieter Abbeel. Combinatorial energy learning for image segmentation. In D. D. Lee, M. Sugiyama, U. V. Luxburg, I. Guyon, and R. Garnett, editors, *Advances in Neural Information Processing Systems 29*, pages 1966–1974. Curran Associates, Inc., 2016. 2

[21] Aljoscha Nern, Barret D. Pfeiffer, and Gerald M. Rubin. Optimized tools for multicolor stochastic labeling reveal diverse stereotyped cell arrangements in the fly visual system. *Proceedings of the National Academy of Sciences*, 112(22):E2967–E2976, 2015. 8

[22] David Novotny, Samuel Albanie, Diane Larlus, and Andrea Vedaldi. Semi-convolutional operators for instance segmentation. In *The European Conference on Computer Vision (ECCV)*, September 2018. 2, 5, 6

[23] O. Ronneberger, P.Fischer, and T. Brox. U-net: Convolutional networks for biomedical image segmentation. In *Medical Image Computing and Computer-Assisted Intervention (MICCAI)*, volume 9351 of *LNCS*, pages 234–241. Springer, 2015. (available on arXiv:1505.04597 [cs.CV]). 1, 3, 5

[24] Uwe Schmidt, Martin Weigert, Coleman Broaddus, and Gene Myers. Cell detection with star-convex polygons. *CoRR*, abs/1806.03535, 2018. 2, 5, 8, 9

[25] Carolina Wählby, Lee Kamentsky, Zihan H. Liu, Tammy Riklin-Raviv, Annie L. Conery, Eyleen J. O'Rourke, Katherine L. Sokolnicki, Orane Visvikis, Vebjorn Ljosa, Javier E.

Irazoqui, Polina Golland, Gary Ruvkun, Frederick M. Ausubel, and Anne E. Carpenter. An image analysis toolbox for high-throughput c. elegans assays. *Nature Methods*, 9(7):714–716, 2012. 2, 6

[26] Martin Weigert, Uwe Schmidt, Robert Haase, Ko Sugawara, and Gene Myers. Star-convex polyhedra for 3d object detection and segmentation in microscopy. *arXiv:1908.03636*, 2019. 2, 5, 8, 9

[27] Steffen Wolf, Constantin Pape, Alberto Bailoni, Nasim Rahaman, Anna Kreshuk, Ullrich Köthe, and Fred A. Hamprecht. The mutex watershed: Efficient, parameter-free image partitioning. In *ECCV (4)*, volume 11208 of *Lecture Notes in Computer Science*, pages 571–587. Springer, 2018. 1, 3, 5, 8, 10

[28] Steffen Wolf, Lukas Schott, Ullrich Kothe, and Fred Hamprecht. Learned watershed: End-to-end learning of seeded segmentation. In *Proceedings of the IEEE International Conference on Computer Vision*, pages 2011–2019, 2017. 1

[29] Victor Yurchenko and Victor S. Lempitsky. Parsing images of overlapping organisms with deep singling-out networks. In *2017 IEEE Conference on Computer Vision and Pattern Recognition, CVPR 2017, Honolulu, HI, USA, July 21-26, 2017*, pages 4752–4760, 2017. 1, 2, 5, 6, 7

PatchPerPix for Instance Segmentation: Supplementary Material

Peter Hirsch* Lisa Mais* Dagmar Kainmueller
Berlin Institute of Health / Max-Delbrueck-Center for Molecular Medicine in the Helmholtz Association
{firstname.lastname}@mdc-berlin.de
*equal contribution, listed in random order

Supplemental Hyperparameter Study on BBBC010: Patch Size

AP_{dsb}	patch size	$avAP_{[0.5:0.05:0.95]}$	$AP_{0.5}$	$AP_{0.6}$	$AP_{0.7}$	$AP_{0.8}$	$AP_{0.9}$
ppp	25x25	0.689	0.890	0.872	0.840	0.710	0.372
ppp+dec	25x25	0.720	0.895	0.877	0.857	0.763	**0.450**
ppp+dec	31x31	0.725	0.911	0.894	0.866	0.779	0.417
ppp+dec	41x41	0.735	**0.934**	0.907	0.890	0.786	0.408
ppp+dec	49x49	**0.736**	0.928	**0.914**	**0.898**	**0.802**	0.409

Table 1: Impact of patch size used in ppp+dec, assessed on BBBC010. All ppp+dec models have similar code size of ∼250, as well as a comparable number of parameters. For ppp+dec, AP at lower thresholds, as well as avAP, tends to increase with larger patch size. This is expected, as larger patches may bridge larger overlaps of instances. However, AP at higher thresholds tends to decrease with larger patch size. This cannot be straightforwardly attributed to higher compression rate, as AP is robust to code size variation at fixed patch size (see Supp. Table 2). We hypothesize that it is due to shape variance increasing with increasing distance from the center pixel of a patch, causing larger patches to yield lower pixel accuracy at the fringes. Furthermore, ppp+dec considerably outperforms ppp at the same patch size (25x25) and same number of parameters. Improvement of ppp+dec over ppp is largest for AP at high thresholds. We hypothesize that this may be due to differences in training procedures, where in ppp+dec, only forground patches contribute to the loss, whereas in ppp, all patches contribute, thereby significantly shifting balance. Said hypotheses have to be verified by further experiments.

Supplemental Hyperparameter Study on BBBC010: Code Size

AP_{dsb}	code size	$avAP_{[0.5:0.05:0.95]}$	$AP_{0.5}$	$AP_{0.6}$	$AP_{0.7}$	$AP_{0.8}$	$AP_{0.9}$
ppp+dec	324	**0.737**	0.931	**0.919**	**0.897**	0.784	0.418
ppp+dec	252	0.735	**0.934**	0.907	0.890	0.786	0.408
ppp+dec	216	0.734	0.922	0.900	0.876	0.793	**0.443**
ppp+dec	180	0.730	0.929	0.914	0.892	0.782	0.401
ppp+dec	144	0.722	0.916	0.893	0.874	0.785	0.402
ppp+dec	108	0.734	0.932	0.914	0.893	0.776	0.409
ppp+dec	72	0.735	**0.934**	0.914	0.894	**0.795**	0.407

Table 2: Impact of code size used in ppp+dec, assessed on BBBC010. Patch size fixed at 41x41, number of parameters kept constant. ppp+dec achieves comparable results across a range of compression rates we assessed.